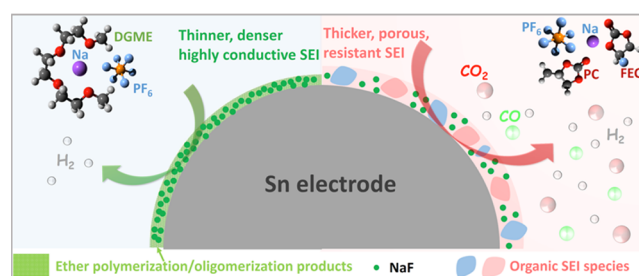


Highly Reversible Sodiation of Tin in Glyme Electrolytes: The Critical Role of the Solid Electrolyte Interphase and Its Formation Mechanism

Bingsheng Qin, Alexander Schiele, Zenonas Jusys, Alessandro Mariani, Thomas Diemant, Xu Liu, Torsten Brezesinski, R. Jürgen Behm, Alberto Varzi,* and Stefano Passerini*

ABSTRACT: Utilization of high capacity alloying anodes is a promising yet extremely challenging strategy in building high energy density alkali ion batteries (AIBs). Excitingly, it was very recently found that the (de)sodiation of tin (Sn) can be a highly reversible process in specific glyme electrolytes, enabling high specific capacities close to the theoretical value of 847 mA h g^{-1} . The unique solid electrolyte interphase (SEI) formed on Sn electrodes, which allows highly reversible sodiation regardless of the huge volume expansion, is herein demonstrated according to a series of in situ and ex situ characterization techniques. The SEI formation process mainly involves NaPF_6 decomposition and the polymerization/oligomerization of the glyme solvent, which is induced by the catalytic effect of tin, specifically. This work provides a paradigm showing how solvent, salt, and electrode materials synergistically mediate the SEI formation process and obtains new insights into the unique interfacial chemistry between Na alloying electrodes and glyme electrolytes, which is highly enlightening in building high energy density AIBs.

KEYWORDS: alkali ion batteries, tin anodes, catalytic effect, SEI formation, interfacial chemistry



1. INTRODUCTION

The implementation of highly efficient and sustainable electrochemical energy storage (EES) devices is of crucial importance for the modern society. Among all EES technologies, alkali ion batteries (AIBs) have drawn the most attention owing to their high energy density and long cycling life. In state of the art AIBs, carbonaceous materials, for example, graphite and hard carbon, are generally adopted as anodes because of their low cost and good cyclability, while metal transition oxides are employed as cathodes because of their relatively high working voltage and reasonable capacities.¹ However, even the most successful and well commercialized AIB technology, that is, lithium ion batteries (LIBs), offer energy density of only about 250 W h kg^{-1} at the cell level and is rapidly approaching their intrinsic limit of about 300 W h kg^{-1} dictated by the use of layered transition oxide cathodes [e.g., LiCoO_2 or $\text{LiNi}_x\text{Co}_y\text{M}_{1-x-y}\text{O}_2$ ($M = \text{Mn}$ or Al)] and graphite anodes.² Apparently, the use of transition metal oxide as cathodes for AIBs is very unlikely to change in the following years. In order to further improve the battery energy density, it is, therefore, imperative to develop anode materials with higher energy density to replace the conventional carbonaceous anodes. In this regard, alloying anodes are quite appealing owing to their higher specific capacity compared with traditional carbonaceous anodes and relatively low working potential.³

Unfortunately though, alloying anodes are in general not compatible with the conventional carbonate electrolytes because of their electrochemically unstable electrode/electrolyte interface.^{4–7} As a result of the huge volume expansion/contraction upon charge/discharge, the formed solid–electrolyte interphase (SEI) rapidly degrades, while a fresh SEI continuously forms cycle by cycle at the newly exposed electrode surface.⁸ This leads to the evolution of flammable gases upon cycling as well as fast electrolyte depletion, raising safety concerns and shortening cell life.⁹ Downsizing active material particles to nanoscale and implementing surface coating have proved to be effective strategies to alleviate the large volume expansion and electrode/electrolyte interfacial instability.^{7,8,10} However, the intricate synthesis processes as well as the decreased tap densities of active materials diminish the application potential of those strategies. For these reasons, despite the tremendous work in the past three decades, alloying anodes have not been used dominantly in AIBs for practical applications up to now.¹¹ Resolving the interfacial instability

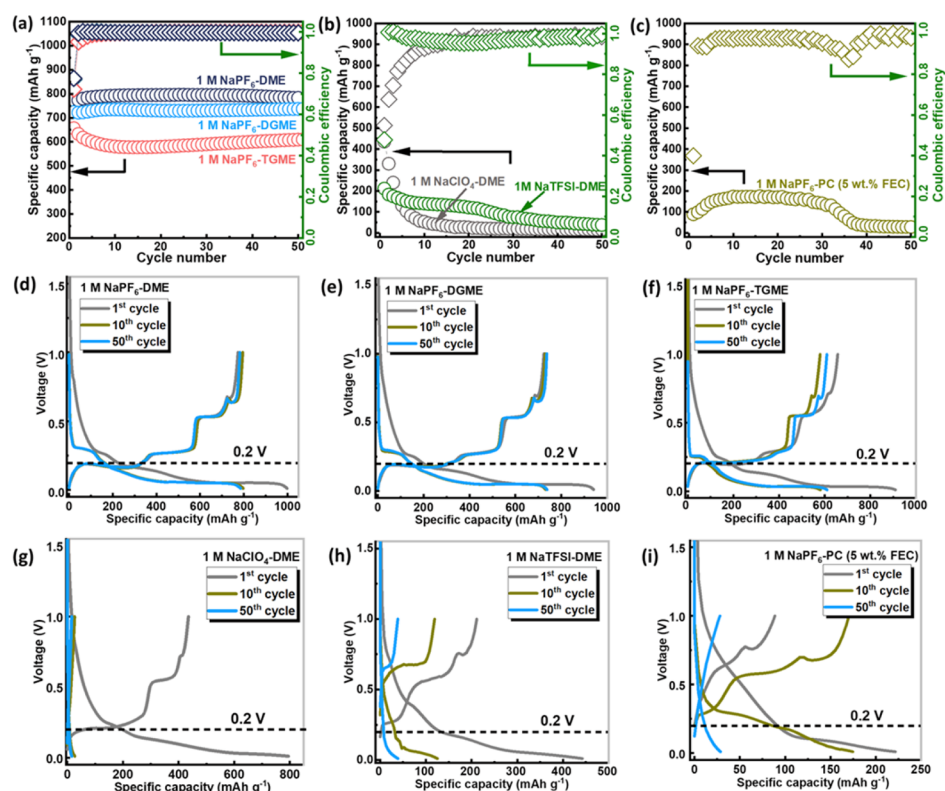


Figure 1. Cycling performance (a–c) and selective voltage–capacity profiles (d–i) of Na/m Sn cells with different electrolytes. The tests were performed at 20 °C at a specific current of 250 mA g⁻¹ in the voltage range between 0.01 and 1 V. Note that PVDF was used as binder in the m Sn electrodes.

between alloying anodes and electrolytes has become an extremely important but rather challenging task in building high energy density AIBs.

A breakthrough work was very recently presented by Zhang et al.,¹² who demonstrated the highly reversible (de)sodiation of micro sized tin (m Sn) based anodes by means of a specific class of glyme electrolytes (1 M NaPF₆–glyme/diglyme/tetraglyme). Specifically, a micro sized (–325 mesh) Sn anode (m Sn), without any sophisticated material or electrode design, was found to exhibit a reversible specific capacity over 800 mA h g⁻¹, a value rather close to the theoretical value of 847 mA h g⁻¹, regardless of the unavoidable large volume expansion upon (de)sodiation.¹² Additionally, an initial Coulombic efficiency of 92% was achieved, which is unprecedentedly high for alloying anodes.^{3,13} Later, it has been demonstrated that a high cyclability (5000 cycles) can be achieved by optimizing the binder, conductive agent, and separator.¹⁴ Meanwhile, following the demonstrated electrochemical performance of Na/Sn half cells, excellent cyclability of the corresponding full cells (Sn/Na₃V₂(PO₄)₃ and Sn/Na₃(VO_{0.5})₂(PO₄)₃F₂) was also achieved by Li and co workers using the same electrolytes. The superior electrochemical performances were ascribed to the self established microporous electrode structure, which can effectively alleviate the volume expansion during cycling.^{15–19} Afterward, Zhang et al. found that the use of such glyme electrolytes promotes fast charge transfer at the SEI/electrode interface.²⁰ In a very recent work, Huang et al. evaluated the properties of the SEI formed on a Sn anode in glyme electrolytes. They could demonstrate that the SEI formed is a rather thin polymeric film but with superior mechanical elasticity and stability, which provides stability against the large volume changes upon (de)sodiation.²¹

Nevertheless, in spite of the above achievements, the intriguing Sn/glyme electrolyte interfacial chemistry is yet to be thoroughly understood. Especially, although the nature of the SEI on the Sn electrode in glyme electrolytes has been well investigated,²¹ the role of the SEI with regard to the superior cell performance as well as its formation mechanism are still largely unknown. Fully clarifying the interfacial (electro)chemistry between Sn anodes and such glyme electrolytes and further exploiting the underlined principle are of fundamental importance to achieve high energy density AIBs. To address these critical points, we herein comparatively evaluate the influence of several factors, including the binder, electrolyte solvent, and salt, on the Sn anode performance, clearly highlighting the critical role of the SEI in enabling highly reversible (de)sodiation of Sn anodes. Thereafter, combining a set of complementary ex situ and in situ techniques, the SEI formation process is comprehensively studied and discussed.

2. RESULTS AND DISCUSSION

2.1. Impact of the Binder and Electrolyte Composition on Na/m-Sn Cell Performance. Two electrode (2032) coin cells were assembled,^{12,14,15} composed of an m Sn electrode as the working electrode and a Na foil the as counter electrode, to evaluate the electrolyte influence on the cell cycling performance. Before discussing the results, one should keep in mind that the electrolyte not only affects the electrochemical behavior of the Sn based cathode but also of the anode (in this case, the Na counter electrode). The latter may have a significant influence on the Na/m Sn cell performance.^{22,23}

The cell cyclability in different kinds of electrolytes is shown in Figure 1a–c. All cells show a stable cycling performance at

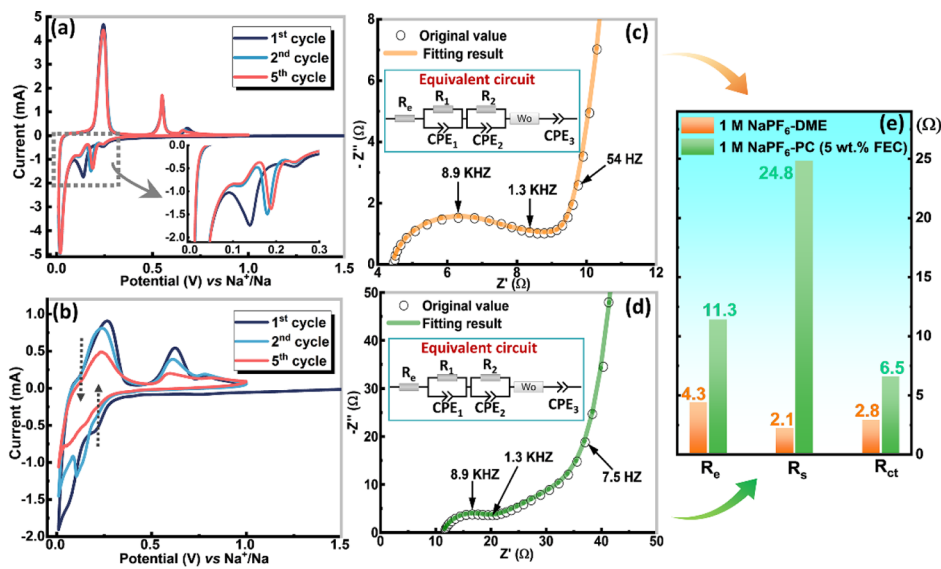


Figure 2. (a,b) CV curves of 3 electrode cells using an m Sn working electrode and a Na foil as the counter/reference electrode (scan rate: 0.05 mV s⁻¹) and (c,d) electrochemical impedance spectra (EIS) of sodiated m Sn/m Sn symmetric cells after five cycles, with fitting results using the equivalent circuit shown in the inset. (e) Comparison of the resistance values obtained from EIS fitting. Electrolytes used: (a,c) 1 M NaPF₆-DME and (b,d) 1 M NaPF₆-PC (5 wt % FEC).

250 mA g⁻¹ up to 50 cycles (Figure 1a), at least, when using electrolytes composed of 1 M NaPF₆ in dimethoxyethane (DME/glyme), diethylene glycol dimethyl ether (DGME/diglyme), and tetraethylene glycol dimethyl ether (TGME/tetraglyme), which is in good agreement with the previous report from Zhang et al.¹² However, it is worth noting that we used a different binder [polyvinylidene fluoride (PVDF)] with respect to Zhang’s paper [carboxymethyl cellulose (CMC)].¹² The rather similar performance demonstrates that the binder does not particularly affect the cell performance, thus excluding its prominent role in achieving high performance Sn anodes.

In addition, the choice of the glyme solvent (DME, DGME, and TGME) has almost no influence on the cell cyclability. In fact, only the obtained specific capacity varies (see Figure 1a). The highest capacity is delivered in the DME based electrolyte, followed by DGME and TGME. This trend can be reasonably ascribed to the increased solvent viscosity (DME < DGME < TGME) slowing down the ionic transport. Anyhow, the cell capacity is well maintained after 50 cycles with all glyme electrolytes, which is clearly illustrated by the almost identical sodiation/de sodiation profiles for the 1st, 20th, and 50th cycle (Figure 1d–f). A striking feature of the cell using 1 M NaPF₆-glyme electrolytes is that a large portion of the capacity is achieved in the low voltage region (0.005–0.2 V, as indicated by the dashed line) (Figure 1d–f), which is characteristic for Sn anodes.¹² In sharp contrast, either changing the salt from NaPF₆ to NaTFSI or NaClO₄ (Figure 1b), or changing the solvent from glyme to carbonate (here propylene carbonate (PC) with 5 wt % fluoroethylene carbonate (FEC) additive) (Figure 1c), leads to a rapid cell failure and extremely low specific capacities (less than 200 mA h g⁻¹) after a few cycles. In other words, both the glyme solvent and the NaPF₆ salt play a decisive role in achieving high performance m Sn anodes. Besides, in comparison with the cells using NaPF₆-glyme based electrolytes (Figure 1d–f), the capacity contribution from the low voltage region (below 0.2 V) is very small and rapidly decreasing after the 1st cycle (Figure 1g–i) in the other electrolytes. This phenomenon is associated to a large extent with the polarization of the Na anode, as

demonstrated by the overpotential of various Na counter electrodes in cell tests (Figure S1) and further supported by electrochemical impedance spectroscopy (EIS) measurements of Na/Na symmetric cells (Figure S2). However, the fast capacity fading observed in a three electrode cell using 1 M NaPF₆-PC (5 wt % FEC) electrolyte demonstrates that the sodium counter electrode polarization is not the decisive reason for the rapid capacity fading of Na/Sn cells (Figure S3).

As evidenced by in situ dilatometry, the m Sn electrode shows a thickness increase of 60% compared with the initial state in the first cycle when using 1 M NaPF₆-DME electrolyte, clearly demonstrating the expected large volumetric expansion (Figure S4). Therefore, the excellent cyclability of the m Sn anode achieved in NaPF₆-glyme electrolytes (Figure 1a) must result from the well stabilized interface between the electrode and this kind of electrolyte.

2.2. Impact of Electrolyte on the m-Sn Electrode/Electrolyte Interface: Electrochemical and Ex Situ Characterization. To gain a better understanding of the impact of the different electrolytes on the performance of the m Sn electrode in Na/m Sn cells, cyclic voltammetry (CV) measurements were performed in 3 electrode cells to highlight the electrochemical response of the m Sn electrode upon a change in cell potential. In the following, to simplify the scenario, 1 M NaPF₆-DME is selected as a representative glyme electrolyte, allowing reversible (de) sodiation of Sn, while 1 M NaPF₆-PC (5 wt % FEC) is picked as representative of “non effective” electrolytes. As shown in Figure 2a, when 1 M NaPF₆-DME electrolyte is used, the voltammograms are overlapping in consecutive scans, indicating of the highly reversible sodiation/(de) sodiation, which is in good agreement with the stable cycling performance discussed previously (Figure 1a,d–f). However, upon closer inspection of the low potential region (inset of Figure 2a), especially between 0.1 and 0.2 V, some small differences are observed between the 1st scan and the later scans. Most strikingly, the major reduction peak appears downshifted in the 1st reduction compared to the subsequent scans but with a higher peak current as well as a larger integrated

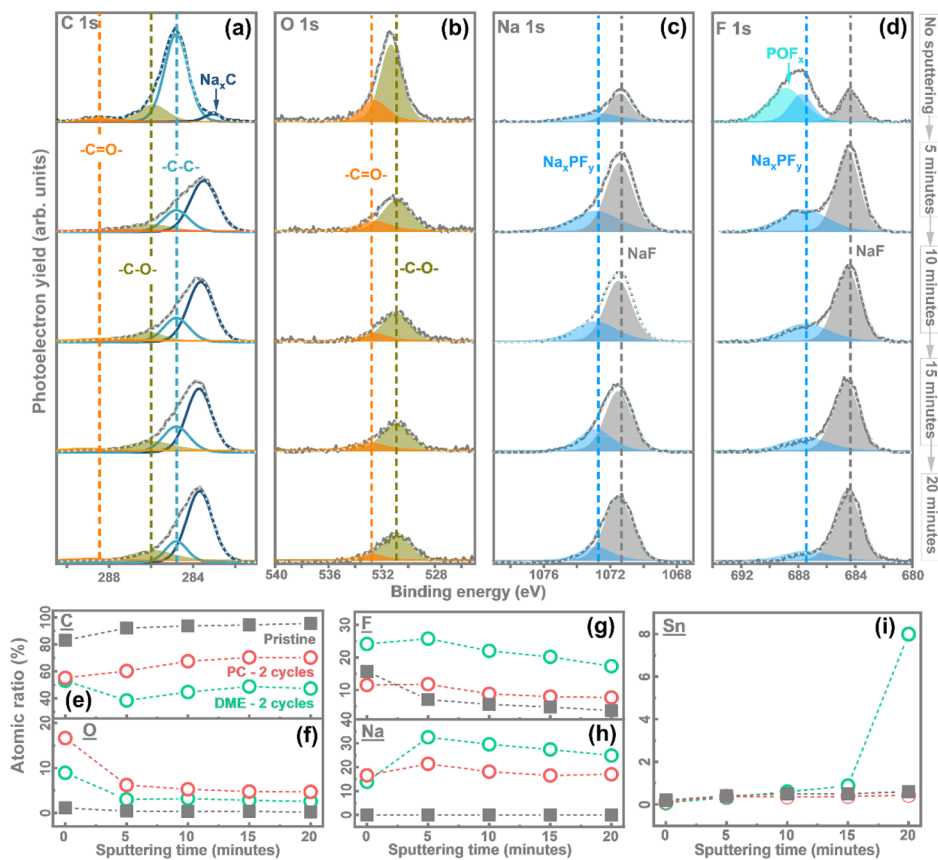


Figure 3. XPS spectra in the (a) C 1s, (b) O 1s, (c) Na 1s, and (d) F 1s regions, collected from an m Sn electrode after two full sodiation/desodiation cycles in 1 M NaPF₆-DME electrolyte. Variation of the atomic concentration of (e) carbon, (f) oxygen, (g) fluorine, (h) sodium, and (i) tin in the surface layer of m Sn electrodes in 1 M NaPF₆-DME or 1 M NaPF₆-PC (5 wt %) electrolytes in comparison with that of a pristine m Sn electrode as a function of the sputtering time.

peak area. This is most probably connected to delayed sodiation as well as the SEI formation process in the initial cycle, although no direct evidence is available here. For the cell using 1 M NaPF₆-PC (5 wt % FEC) electrolyte, the current-potential profiles are largely different (Figure 2b). First, the current of almost all the peaks is substantially lower, whereas the peaks are correspondingly broader, demonstrating a lower (de)sodiation rate. In addition, the peak currents are continuously decreasing during cycling, indicative of severe capacity loss, which again agrees well with the corresponding galvanostatic cycling results (Figures 1c,i and S3).

To further elucidate the m Sn electrode/electrolyte interfacial properties, symmetric cells were prepared composed of one fresh and one pre sodiated m Sn electrodes. The EIS spectra of the cells after five cycles are shown in Figure 2c,d. In such cell configuration, the impedance contribution from the sodium electrode can be excluded, and the impedance information solely results from the m Sn electrode and the electrolyte, including their interface. A rough look reveals similar sodiation/desodiation profiles for both electrolytes, as shown in Figure S5. However, the corresponding EIS spectra show substantially different medium-high frequency semicircles both in open circuit voltage (OCV) prior to cycling (Figure S6) and after five charge-discharge cycles (Figure 2c,d). The impedance spectra after five cycles were fit using a typical equivalent circuit composed of the following elements: electrolyte resistance (R_e), SEI impedance (R_1 and CPE_1), charge transfer impedance (R_2 and CPE_2), and the Warburg impedance (W_o) accounting for

the Na⁺ ion diffusion and the constant phase element (CPE_3) accounting for the capacitive charge accumulation in the electrode.²⁴ As shown in Figure 2e, the spectrum obtained in 1 M NaPF₆-DME electrolyte features an SEI resistance of 2.1 Ω and a charge transfer resistance of 2.8 Ω , which is significantly smaller than those using 1 M NaPF₆-PC (5 wt % FEC) electrolyte (24.8 and 6.5 Ω , respectively). This indicates fast Na⁺ transport through the SEI as well as rapid charge transfer at the m Sn electrode/glyme electrolyte interface, which nicely fits the outstanding rate capability shown in Figure S7.

The surface chemistry of the m Sn electrode after two cycles in the glyme electrolyte was investigated by ex situ XPS measurements. Ar⁺ ion sputtering was used for depth profiling to gain a comprehensive understanding of the elemental composition and the chemical environment of the elements in the SEI layer.^{25,26} As demonstrated by the C 1s, O 1s, Na 1s, and F 1s spectra after different sputtering times (Figure 3a-d), the m Sn electrode's surface in 1 M NaPF₆-DME electrolyte is clearly covered by some SEI related compounds. More specifically, the C 1s spectrum (Figure 3a) evidences the presence of different species with binding energies (BEs) of \sim 286 and \sim 288.5 eV, in addition to the unsodiated (-C-C-) and sodiated (Na_xC) conductive carbon additive. Furthermore, it is interesting to note that the characteristic peak of the CF₂ groups in the PVDF binder at \sim 291 eV²⁷ is not observed in the spectra. The absence of this feature in all C 1s spectra (after different sputtering times) further evidences that the m Sn electrode is fully covered by SEI species. The peaks at \sim 286 and

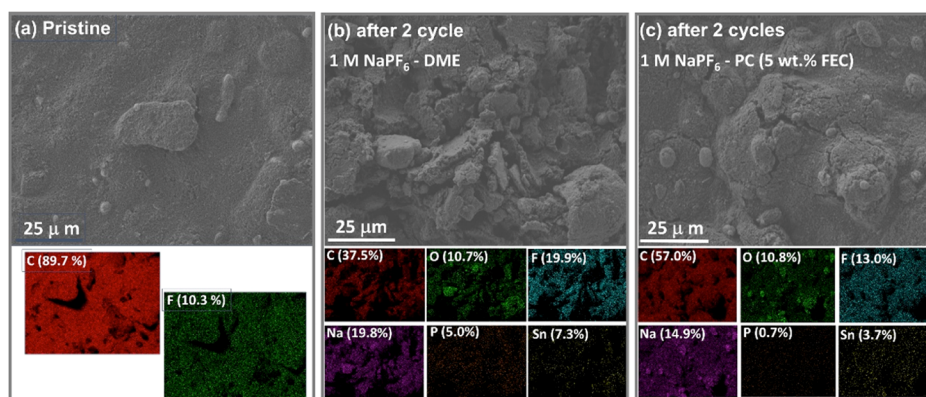


Figure 4. SEM images and corresponding EDX spectra obtained from an m Sn electrode (a) in the pristine state and (b,c) after two full cycles using (b) 1 M NaPF₆-DME and (c) 1 M NaPF₆-PC (5 wt % FEC) electrolytes, respectively.

~288.5 eV can be related to chemical bonding between carbon and oxygen. More precisely, according to our previous work, these two peaks can be ascribed to C–O (R–O–Na/R–O–R, etc.) and C=O (R–O–CO₂–Na, etc.) species, respectively, which is in agreement with the O 1s region spectrum.²⁸ In the F 1s and Na 1s region (Figure 3c,d), the spectra are dominated by peaks that can mainly be assigned to NaF resulting from NaPF₆ decomposition. Additionally, some other sodium salts species (like Na_xPF_y) could be detected. Overall, the in depth ex situ XPS analysis clearly identifies the SEI formation on the m Sn electrode surface in the glyme electrolyte.

To gain a better understanding of the SEI composition, we compared the results of the quantitative XPS elemental analysis of pristine and cycled electrodes in different electrolytes. Scanning electron microscopy (SEM) and corresponding energy dispersive X ray spectroscopy (EDX) images of these electrodes are shown in Figure 4. The evolution of the atomic concentrations as a function of sputtering time is shown in Figure 3e–i. At any sputtering stage the pristine m Sn electrode is mostly composed of carbon and fluorine, while the concentrations of oxygen and Sn are very low, which agrees well with the SEM–EDX mapping results of the pristine electrode (Figure 4a). These results indicate that the m Sn particles are covered by a relatively thick layer of conductive carbon and a PVDF binder. For the cycled samples, the carbon content decreases substantially after two cycles, while that of oxygen, fluorine and sodium increases significantly, resulting from the SEI formation with both electrolyte types. Furthermore, we note that the content of O and C on the m Sn electrode is much lower over the entire sputtering time in 1 M NaPF₆-DME electrolyte than that in the PC based electrolyte (Figure 3e,f), while the contents of Na and F are higher (Figure 3g,h). This, again, agrees well with the EDX mapping data (Figure 4b,c), which show more Na, F, and P in the electrode surface region after cycling (two cycles) in glyme electrolytes but significantly less C and Sn. These results strongly indicate that in 1 M NaPF₆-DME electrolyte, the SEI arises more from the decomposition of the salt (NaPF₆), while it is more composed of solvent derived products for the carbonate based electrolyte. This conclusion is supported also by density functional theory (DFT) calculations showing that the reduction of glyme related species is very unlikely in the voltage range of a working Na/m Sn battery (0.01–1 V), while the reduction of both PC and FEC is possible (see Tables S1 and S2).

It is worth pointing out that the increased amount of oxygen on the m Sn electrode in the glyme electrolyte, compared with

the pristine electrode, cannot be related to the residual DME solvent because of its high volatility leading to removal upon the vacuum step prior to the XPS measurement. Also, it cannot be due to the fragmentation products of DME either, as explained later in the In Situ DEMS section. Finally, it cannot be related to the binder, as PVDF is used here instead of CMC. Considering that the glyme solvent is the only species containing oxygen in the electrode and electrolyte, the increased amount of oxygen in the SEI can only be due to oligomerization/polymerization of the glyme solvent. Of importance, the increase of the oxygen content can already be observed after the OCV step indicating SEI formation to occur even before cell cycling (Table S3).

Finally, it should be noted that the surface Sn content of the electrode cycled in the glyme electrolyte increases significantly after 20 min sputtering (Figure 3i), while the electrode cycled in the carbonate electrolyte does not show any change at this point. Furthermore, the EDX mapping shows a higher Sn content for the sample cycled in the glyme electrolyte (Figure 4b,c). Altogether, these results indicate that the SEI layer formed when using the glyme electrolyte is relatively thin.

2.3. Gas Evolution at the m-Sn/Electrolyte Interface: In Situ DEMS and OEMS Study. The EIS, XPS, and SEM–EDX results unambiguously evidence the formation of an inorganic compound rich SEI on m Sn electrodes when using 1 M NaPF₆-DME electrolyte, which appears to be the key enabler for the highly reversible electrochemical (de)sodiation behavior. Thus, understanding its formation process is of utmost importance. In recent years, online electrochemical mass spectrometry (OEMS) has often been employed to investigate the gaseous species evolving during electrochemical cycling. This technique combined with, for example, ex situ XPS can provide complementary information in order to comprehensively elucidate the interfacial processes.²⁹ However, in most of the OEMS measurements, a carrier gas is used (e.g., helium), and all gases evolving in the cell, both from cathode and anode side, are collected for the subsequent mass spectroscopic analysis, making the independent evaluation of the gassing behavior of each individual electrode impossible.^{4,29,30} In our present work, for example, we are particularly interested in the gas evolution during the SEI formation process at the m Sn/electrolyte interface only. In order to achieve this goal, a recently developed novel differential electrochemical mass spectrometry (DEMS) approach was employed, allowing the selective monitoring of gas evolution at the m Sn electrode/electrolyte interface during cell cycling.³¹ Briefly, the m Sn based slurry was directly casted on a non porous, Cu sputtered fluorinated

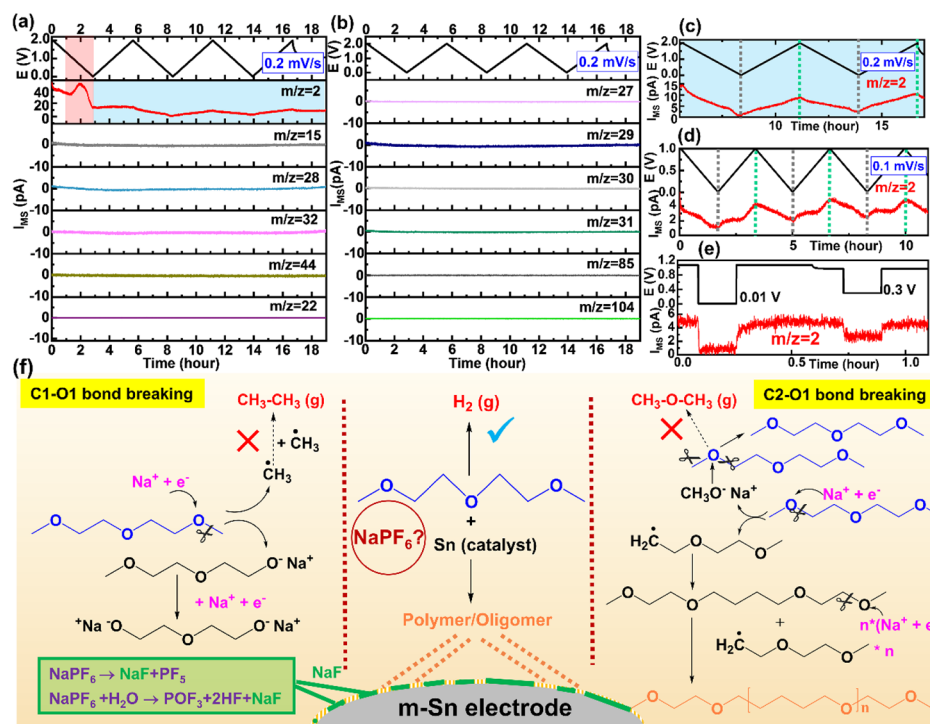


Figure 5. (a,b) Ion current evolution acquired from DEMS measurements of gaseous species with different m/z ratios as a function of time (scan rate: 0.2 mV s^{-1}) during (de) sodiation of m Sn electrodes. (c) Magnified view on the right shadowed section in (a). (d) DEMS response of H₂ at a low scan rate of 0.1 mV s^{-1} . (e) Potentiostatic sodiation profiles of a cell and corresponding mass spectrum for $m/z = 2$. (f) Schematic illustration of the reaction routes for gas production at the m Sn electrode/glyme electrolyte interface. 1 M NaPF₆-DGME was used as an electrolyte, while a sodium strip served as counter and reference electrodes. Note: the ion current values of the DEMS signal are always relative to the lowest value in the same panel rather than absolute numbers; the same for the following section.

ethylene propylene (FEP) membrane, which is directly connected to a vacuum pump transferring the gas for subsequent mass spectrometry analysis. As demonstrated in our previous work,³¹ this special configuration allows selective detection of gases evolving at the working electrode/electrolyte interface, while detection of gases from more distant areas, for example, from the counter electrode, is inhibited. To the best of our knowledge, we are the first to employ this kind of technique to investigate the interfacial processes between alloying anodes and different electrolytes. It should be noted that for this type of experiments, 1 M NaPF₆-DGME was used as the electrolyte because DME is highly volatile and may lead to fast electrolyte depletion and cell failure.

The CVs performed using the cell setup for DEMS measurements, involving an m Sn based working electrode, are shown in Figure S8. Different from the CVs of conventional T cells (see Figure 2a), a substantial decay of the current density is observed after the 1st cycle when using 1 M NaPF₆-DGME electrolyte, most likely due to the electrode material delamination. Overall, as shown in Figure 5a,b, only the periodic evolution of H₂ ($m/z = 2$) can be detected upon sodiation and de sodiation, while that of the other gas species is featureless, as shown in Figure 5a,b. To be more specific, upon the first sodiation of the m Sn electrode, a notable amount of H₂ gas is produced (see the red shadowed section) at a potential around 0.2 V versus Na/Na⁺. This is most probably related to the reduction of H₂O impurities in the electrolyte, as suggested by its absence in the following cycles. Afterward, the H₂ evolution follows a periodic, potential dependent pattern, reaching maximum and minimum values at the upper cut off potential (2 V) and lower cut off potential (0.01 V), respectively, as can be

clearly seen in the magnified image (Figure 5c). Such a periodic trend was further confirmed in a subsequent measurement at a lower scan rate (0.1 mV s^{-1} , see Figure 5d). It is worth noting that the result obtained at the m Sn electrode/electrolyte interface largely resembles that from a conventional OEMS measurement (Figure S9) in which gaseous products from both electrodes were collected and, still, only H₂ evolution was unambiguously evidenced. This indicates either similar gas evolution processes at both electrodes or negligible gas production at the Na metal electrode side. The potential dependent gassing behavior is further confirmed in the potentiostatic mode DEMS measurement. As shown in Figure 5e, a lower H₂ amount is detected when the electrode potential is held at 0.01 V, while it increases to a higher value at 0.3 V. It should be particularly noted that the gas formation responds instantaneously to the potential variation in the potentiostatic mode, demonstrating that the time constant of the detection is short and the H₂ evolution is a strictly potential dependent process. To be more specific, with increasing potential more H₂ is produced. Considering that the electrochemical reduction of moisture in the cell system is generally an irreversible process and that DGME is the only species in the cell that contains hydrogen, it is reasonable that H₂ gas is mostly produced as a byproduct of the ether solvent polymerization/oligomerization. This is in line with the increased amount of oxygen species (C-O, C=O, etc.) on the m Sn electrode observed after two cycles according to the ex situ XPS measurement (Figure 3). Also, the periodic H₂ evolution is missing in 1 M NaPF₆-PC (5 wt %) electrolyte (to be discussed later). Such an argument nicely fits the results of Huang et al. who evidenced, in a very recent work,²¹ the existence of mechanically elastic and stable polymer

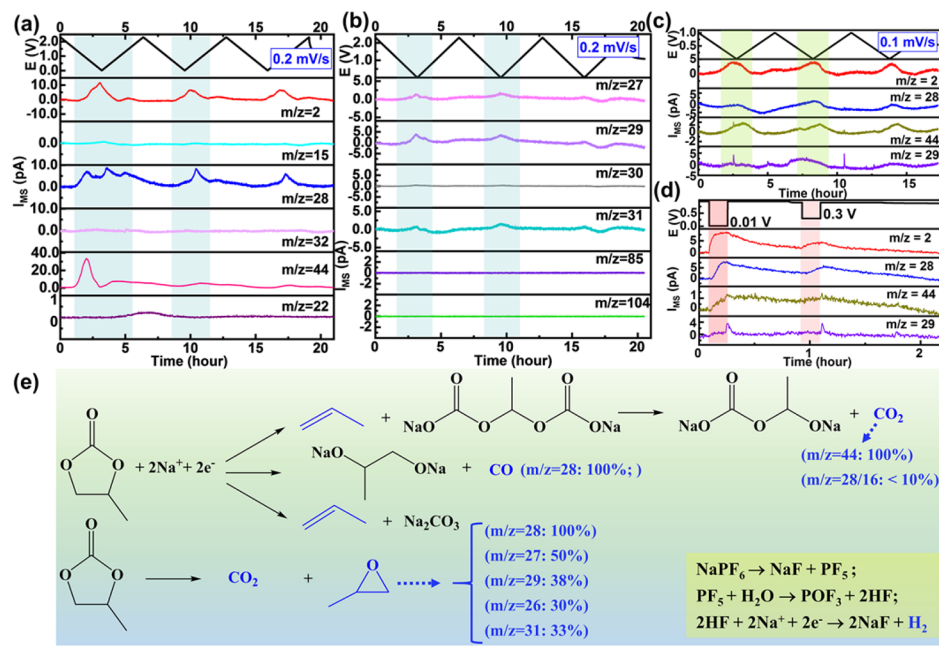


Figure 6. (a,b) Mass signals for gases with different m/z ratios as a function of time (scan rate: 0.2 mV s^{-1}) from se DEMS. (c) DEMS response of several selected gas species at a lower scan rate of 0.1 mV s^{-1} . (d) Potentiostatic sodiation profiles of the m Sn electrode and corresponding mass spectra for selected gas species. $1 \text{ M NaPF}_6\text{-PC}$ (5 wt % FEC) was used as an electrolyte while a sodium metal strip served as counter and reference electrodes, respectively. (e) Carbonate solvent decomposition routes.

like species in this SEI layer by in situ atomic force microscopy (AFM). Worth to notice, the contribution of the ether solvent decomposition in the formation of nongaseous products cannot be excluded according to the experimental results here and in previous works.^{21,32} However, the fragmentation of the ether solvent can be excluded as no signal for volatile compounds (Figures S10–S13) can be evidenced here. It should be also noted that with the same electrolyte such potential dependent H₂ evolution is not observed in a parallel DEMS measurement for microsized antimony (m Sb) electrodes (Figure S14), highlighting the critical role of Sn in the SEI formation process. The “Sn assisted” SEI formation process explains why some alloying anodes can be reversibly (de)sodiated while others cannot (Figure S15). Most probably, Sn species serve as catalysts for the ether polymerization/oligomerization.

It is worth noting that changing the electrolyte salt from NaPF₆ to NaTFSI or NaClO₄ will also lead to rapid cell failure, indicating that NaPF₆ also plays a key role, that is, the SEI formed in this regard is co modulated by a solvent, salt, and electrode material. Although the catalytic effect of Sn on carbonate electrolyte decomposition is well documented,^{33,34} this is the first time that its catalytic effect is evidenced for glyme solvent polymerization/oligomerization, which contributes to the formation of a highly effective SEI, thus opening new opportunities for building high performance AIBs. Of note, different from most of work that stress only the contribution of solvents or salts (or additives) in the SEI formation process,^{35–38} our disclosed SEI formation route highlights the synergistic contribution of solvent, salt, and electrode materials in this course. In addition, the rapid gas formation rate change clearly demonstrates the reliability of our novel DEMS measurement in capturing individual gases locally at one electrode. In general, gas diffusion from the counter/reference electrode to the working electrode takes longer time and leads to a delay in gas detection, which is not the case in the potentiostatic measurement shown here (Figure 5e).

Finally, the possible reaction routes for gas production at the m Sn electrode/glyme electrolyte interface are illustrated in Figure 5f. In general, the chemical bond between the edge oxygen atom and the neighboring carbon atom is relatively prone to cleavage (C1–O1 and C2–O1),²¹ leading to the formation of radical species. The formed radicals may further induce solvent decomposition and subsequent polymerization, especially with the assistance of Lewis acids from the decomposition products of NaPF₆. However, one should keep in mind that in both cases, gaseous products (CH₃–CH₃ or CH₃OCH₃) will be formed simultaneously.^{21,32} Nevertheless, their relevant mass signals were not detected in the DEMS measurement ($m/z = 28, 27, 26$ for CH₃–CH₃ and $m/z = 29, 15$ for CH₃OCH₃). This indicates an alternative reaction route for SEI formation, which, as we demonstrated, involves Sn induced ether polymerization/oligomerization (here the role of NaPF₆ remains elusive) and NaPF₆ decomposition.

For the carbonate electrolyte (CV shown in Figure S16), the most striking difference in the gassing behavior (Figure 6a,b) is that the highest gas formation rate is always obtained at the lowest potential, while the lowest gas concentration is at the highest potential, which is opposite to the glyme electrolyte system. This result is confirmed also in the slow scanning mode (Figure 6c) and potentiostatic scanning mode (Figure 6d). In addition, the resulting gas species are substantially different. Namely, CO₂ ($m/z = 44$) and others are formed in addition to H₂ upon the carbonate solvent decomposition (Figure 6e) during the SEI formation process.^{4,33,39} It should be noted that, although CO₂ evolution in a conventional full cell OEMS measurement shows the same trend as in DEMS, the H₂ evolution pattern is completely different, indicating that a sizable amount of H₂ is generated at the Na counter electrode in the end of the de sodiation process (Figure S17). Overall, the fact that much more gas is formed in this case must be associated with more substantial parasitic reactions at the Sn electrode/

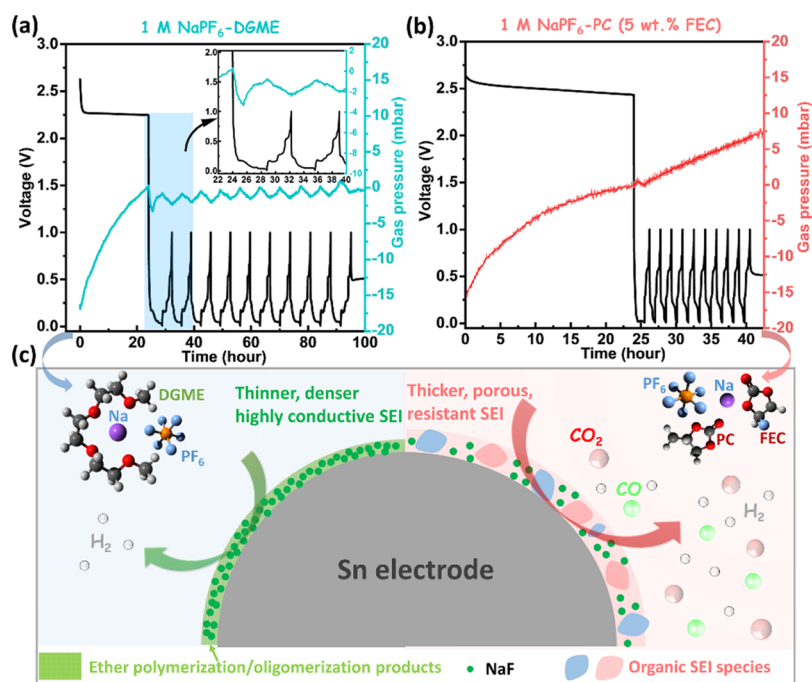


Figure 7. (De)sodiation profiles and the corresponding pressure curves for Na/m Sn batteries using (a) 1 M NaPF₆-DGME and (b) 1 M NaPF₆-PC (5 wt % FEC). Figure (c) shows the corresponding schematic illustration of the interfacial gassing processes between the Sn electrode and different electrolytes.

carbonate electrolyte interface, indicating that an effective SEI is not formed.

2.4. Impact of the Electrolyte on the Na/Sn Cell Gassing Behavior. Gassing is one of the most common phenomena in batteries, being the result of unavoidable parasitic reactions at the electrode/electrolyte interfaces including but not limited to the SEI formation.^{4,30} Ideally, gas evolution should be limited to the 1st cycle after which an effective SEI formation should prevent further side reactions. Therefore, the gas pressure evolution in a battery can be used as an indicator for the amount of detrimental side reactions.⁴

Figure S18 shows the cell performance of custom made two electrode cells used for pressure measurements. The Na/m Sn cell shows a cyclability similar to that of conventional two electrode coin cells (see Figure 1), demonstrating the reliability of the system. The corresponding pressure evolution profiles are depicted in Figure 7a,b. Specifically, both cells (with different electrolytes) experienced a relatively large pressure increase during the OCV period, suggesting the onset of SEI formation on the electrodes. This is partly supported by the electrochemical impedance evolution in the OCV state obtained on a Na/Na symmetric cell (Figure S2). A semicircle at high to medium frequencies, which is usually considered as indicative of the existence of a SEI film, is clearly detected and slightly evolves upon cell wetting/storage.

After the OCV period, the pressure curves show a distinctly different overall trend upon electrochemical (de)sodiation when using glyme or carbonate based electrolytes. In the case of 1 M NaPF₆-DGME electrolyte, the pressure is mostly stable without a significant increase over cycling. However, a closer look reveals some interesting features. Upon sodiation, the pressure in general increases slightly, while it decreases again during desodiation. In total, the pressure varies within a rather narrow range. Such periodic pressure evolution is in contrast to the gassing behavior seen by DEMS and conventional full cell

OEMS measurements in which the maximum value of H₂ gas generation is always reached at the upper cut off potential (Figures 5 and S8). From our point of view, the different finding in this measurement is most presumably related to the volume changes of the Sn electrode upon (de)sodiation. Specifically, in the sodiation/de sodiation upon (de)sodiation process, the Sn electrode expands/shrinks; therefore less/more space is available for the gas in the cell, leading to the pressure increase/decrease, while the additional H₂ production at the m Sn electrode/glyme electrolyte interface is negligible during cycling and cannot be detected in this setup. In addition, a peculiar feature is noticed in the pressure data for the 1 M NaPF₆-DGME electrolyte. As shown in the inset of Figure 7a, at the very beginning of the first sodiation process the gas pressure decreases, which is opposite to the pressure evolution in the following cycles. This finding might be related to the SEI formation process, as it corresponds well to the irreversible cathodic peak in the first CV cycle (Figure 2a). Overall, no significant pressure increase is observed in 10 cycles, at least, indicating rather minor parasitic reactions between the electrode and the glyme based electrolyte, that is, a highly effective SEI is established both on the Na counter electrode and on the m Sn working electrode. In sharp contrast, the pressure keeps increasing during cell cycling when using the carbonate based electrolyte, suggesting more severe parasitic reactions, which negatively affects the cell performance. The periodic (zigzag) pressure evolution is not visible in this case, most probably fully covered by the massive gas evolution from the continuous parasitic reactions (Figure 7c).

3. CONCLUSIONS

In this work, we have investigated the highly reversible sodiation/desodiation behavior of m Sn in glyme based electrolytes and compared it to that of a carbonate based electrolyte. Combining several highly complementary in situ and ex situ techniques, we demonstrate that the SEI formation in 1 M

NaPF₆-glyme electrolyte is a solvent, salt, and electrode material co modulated process. It includes decomposition of NaPF₆, accompanied by polymerization of the solvent, where we propose that the latter is catalyzed by the Sn electrode. The resulting SEI is highly compact and ionically conductive, which can effectively alleviate the parasitic reactions, thus promoting an excellent cyclability and rate capability. In contrast, no effective SEI is established on the m Sn electrode when using the PC based electrolyte, leading to continuous side reactions and therefore poor cycling performance. This study provides a paradigm to demonstrate how the SEI manipulates the cell performance and put one step forward in understanding the intriguing interfaces between Na alloying electrodes and glyme electrolytes, which is highly enlightening in building high energy density AIBs.

4. EXPERIMENTAL SECTION

4.1. Electrode Preparation and Cell Assembly/Tests. To prepare the m Sn based electrodes, 800 mg Sn (Alfa Aesar, 325 mesh, ≥99.8%) and 200 mg conductive carbon black (TIMCAL Super C65) were first mixed using a planetary ball mill, with a ball to powder mass ratio of 10:1. The obtained Sn-C powder was then mixed with a PVDF binder (Solef 6020, Arkema Group) at a mass ratio of 90 to 10 in a suitable amount of *N* methyl 2 pyrrolidone (NMP, Alfa Aesar, anhydrous, ≥99.5%) using a magnetic stirrer to prepare a slurry. Afterward, the slurry was doctor blade casted on a dendritic Cu foil and then dried in an oven at 80 °C for 3 h. The obtained m Sn electrodes were punched into 12 mm diameter discs before drying them in a high vacuum glass oven for 12 h at 100 °C. Thereafter, they were weighed in a dry room (dew point < -70 ppm) before transfer into the glovebox for cell assembly. The preparation of the m Sb electrode was similar to that of the m Sn electrode, with Sn powder being replaced by micro-sized Sb powder (Alfa Aesar, 100 mesh, 99.5%).

The cell assembly was performed in an ultrapure argon filled glovebox (MBraun UNILab, H₂O and O₂ content < 0.1 ppm). For the cell performance evaluation, 2032 type two electrode coin cells were utilized with a Na foil (12 mm diameter) as the counter electrode, m Sn as the working electrode, and a GF/A Whatman membrane (16 mm diameter) as the separator. 1 M NaPF₆ in DME, DGME, and TGME, 1 M NaPF₆ in PC with 5 wt % FEC, 1 M NaTFSI-DME, and 1 M NaClO₄-DME were used as electrolytes for comparing their influence on the cell performance. If not specified, all cells were cycled between 0.01 and 1 V, using a specific current of 250 mA g⁻¹ on a Maccor 4300 battery tester in a 20 °C climate chamber.

Symmetric Na/Na and sodiated m Sn/m Sn cells were assembled using the same method but replacing the Sn working electrode with a Na foil and the Na foil with a presodiated Sn electrode (Na_xSn//Sn cells), respectively. 1 M NaPF₆-DME or 1 M NaPF₆-PC (5 wt % FEC), respectively, served as the electrolyte. The symmetric cells were tested on a VMP3 multichannel potentiostat (Bio Logic, France) using a discharge/charge current of 200 μA, with both the discharge/charge processes lasting 30 min (within the voltage cut off between 2 and -2 V). During cycling of the symmetric cells, electrochemical impedance spectra were recorded after every five cycles in the charged state in the frequency range between 1 MHz and 100 mHz and with an amplitude potential of 5 mV.

Swagelok type cells were assembled for auxiliary cell tests using m Sn as the working electrode and Na foil as the counter and reference electrodes. Both the potential of the working electrode and the counter electrode relative to that of the reference electrode were monitored with the assistance of an auxiliary cable. 1 M NaPF₆-DME electrolyte (100 μL) was added between the working and counter electrodes while 50 μL of electrolyte to the reference electrode side. The same cell configuration was adopted for CV measurements in the range between 0.01 and 2 V versus Na⁺/Na with a sweep rate of 0.1 mV s⁻¹.

4.2. In Situ Dilatometry Measurement. The thickness change of the m Sn electrode layer during sodiation and desodiation was measured with an ECD 3 nano electrochemical dilatometry cell (EL

CELL GmbH). The cell uses a robust but porous ceramic separator, which was thoroughly dried in a vacuum oven overnight at 60 °C before transfer into the glovebox. 1 M NaPF₆-DME electrolyte (250 μL) was injected into the cell to fully wet the working electrode. Finally, it was tested in a 20 °C climate chamber in the potential range from 0.01 to 1.0 V versus Na⁺/Na and at a specific current of 250 mA g⁻¹.

4.3. OEMS, DEMS, and In Situ Pressure Measurements. In situ gas analysis was performed by OEMS and DEMS; in situ pressure measurements were performed using a two electrode cell system. The setups used for OEMS and in situ pressure measurements were described previously in refs 40–42. Custom cells were assembled in an argon filled glovebox. The m Sn electrodes having areal loadings of about 2.0 mg cm⁻² (pressure measurements), 1.8 mg cm⁻² (OEMS, using 1 M NaPF₆-DGME electrolyte), and 1.2 mg cm⁻² (DEMS, using 1 M NaPF₆-PC (5 wt % FEC) electrolyte) were used as the working electrode (30 mm diameter with a 4 mm hole in the center for proper gas extraction), and the Na foil of diameter 32 mm served as the counter and reference electrodes. Two pieces of GF/A of diameters 40 mm (pressure measurements) and 42 mm (OEMS), soaked with 700 μL of electrolyte, were used as a separator. A constant carrier gas flow (2.5 mL_{He} min⁻¹, purity 6.0) was applied during OEMS measurements for gas extraction. The gas was analyzed via mass spectrometry (GSD 320, OmniStar Gas Analysis System, Pfeiffer Vacuum GmbH). After each run, a calibration gas of known composition was introduced to quantify the measured ion currents of H₂ and CO₂. During in situ pressure measurements, the internal cell pressure was recorded using a PAA33X V 3 pressure sensor (Omega). Both in situ pressure measurements and OEMS measurements were conducted at 25 °C.

The novel DEMS measurement was introduced recently and its working principles demonstrated successfully.³¹ In the present work, an m Sn based slurry (Sn/C/PVDF = 72 wt %:18 wt %:10 wt %) was “doctor blade” casted onto a nonporous 50 μm thick FEP polymer film (Bohlender), which was vacuum sputtered with copper before to produce a 40 nm thick copper sublayer. After drying the obtained wet film in an oven at 80 °C for 3 h and then in a high vacuum glass oven at 100 °C for 12 h, it was pressed by a hydraulic press (about 1 min at 2 tons per cm²) to obtain an adherent film of the active material. Working electrodes of 13 mm in diameter were punched from the active material coated membrane, further dried at 100 °C under vacuum and stored in the glovebox under argon (MBraun LabMaster, water, and oxygen content < 0.5 ppm). Before assembling the cells, the electrode discs were additionally dried on a hot plate in the glovebox at 100 °C for about 30 min. The working electrode was installed in a PEEK u cup and pressed by a PEEK cylinder via the Teflon gasket against a steel frit, all located in the Swagelok housing, for interfacing the back side of the membrane to the vacuum system of the mass spectrometer (Pfeiffer Vacuum QMA 410).

The Na metal stripes serving as counter and reference electrodes were cut from the Na foil (≥99.8%, Acros Organics), separated by the T shape Teflon plate and contacted to Cu wires from the opposite sides. The counter reference electrode assembly was immersed into 0.5 mL of the corresponding electrolyte (1 M NaPF₆-DGME or 1 M NaPF₆-PC (5 wt % FEC)), which was pipetted before into the PEEK cell and sealed at the top using Parafilm. The contact wires from the working, counter, and reference electrodes were connected to the corresponding terminals of the potentiostat (PAR 263A) to monitor the open circuit potential (OCP) until it leveled to a constant value of about 2.2 V (typically, 4–5 h). At the same time, the ion currents of 12 selected mass to charge ratios (*m/z* = 2, 15, 22, 27, 28, 29, 30, 31, 32, 44, 85, 104), which may relate to fragments of the electrolyte components and possible decomposition products, were monitored to achieve constant background signals.

After a few potentiodynamic scans at a scan rate of 0.2 mV s⁻¹ in the potential range from 2.2 to 0.01 V versus Na⁺/Na, potentiodynamic measurements were performed scanning from the OCP to 0.01 or 0.3 V (with a 600 s CV step) and then back to the OCP. During these potentiodynamic scans, the mass spectrometric signals of the selected ion currents were simultaneously recorded. Finally, potentiodynamic scans at 0.1 mV s⁻¹ were performed in the potential range from 1.0 to 0.01 V versus Na⁺/Na, while the selected ion currents were monitored.

4.4. Ex Situ SEM–EDX and Ex Situ XPS Measurements. Prior to these ex situ measurements, the Sn electrodes were first sodiated and de sodiated at 250 mA g⁻¹ for two cycles and left at 1 V for 6 h in a Swagelok type cell. Afterwards, the cell was immediately removed from the Maccor and transferred into the glovebox for cell disassembly. The electrode obtained was rinsed with DME for 3 times and then dried in the evacuated antechamber for 30 min. Finally, the m Sn electrode was transferred into the SEM or XPS instrument using dedicatedly designed, well sealed vessels to avoid potential contamination by air.

The morphology of the Sn electrode after two cycles was examined by SEM (ZEISS 155VP field emission scanning electron microscope operated at 3 kV) equipped with EDX. XPS measurements were conducted on a PHI 5800 Multi Technique ESCA instrument (Physical Electronics, USA) at a detection angle of 45° and using pass energies at the analyzer of 29.35 and 93.9 eV for detail and survey measurements, respectively. Most of the spectra were recorded using Al K α radiation, the spectra in the O 1s region, however, were obtained by extra measurements with Mg K α radiation to derive the correct oxygen concentration because the integration of the spectra with Al K α radiation will give an overestimated value due to the interference with the Na KLL Auger signals. Spectra were recorded on the unmodified surfaces and after repeated Ar⁺ ion sputtering (5 kV, 1 μ A) for 5 min, arriving at total sputtering times of 0, 5, 10, 15, and 20 min. The nominal sputter rate (given by the instrument manufacturer) is \sim 1 nm min⁻¹. For BE calibration, the F 1s peak of NaF was set to 684.3 eV. XPS spectra after different sputtering times were collected to investigate the in depth surface chemistry of the m Sn electrodes in different electrolytes. Peak fitting was done using the CasaXPS software package (Shirley background subtraction; peak shape: 70% Gaussian/30% Lorentzian).

■ AUTHOR INFORMATION

Corresponding Authors

Alberto Varzi – Helmholtz Institute Ulm (HIU)
Electrochemical Energy Storage, Ulm, Germany, and
Karlsruhe Institute of Technology (KIT), Karlsruhe,
Germany; orcid.org/0000-0001-5069-0589;
Email: alberto.varzi@kit.edu

Stefano Passerini – Helmholtz Institute Ulm (HIU)
Electrochemical Energy Storage, Ulm, Germany, and
Karlsruhe Institute of Technology (KIT), Karlsruhe,
Germany; orcid.org/0000-0002-6606-5304;
Email: stefano.passerini@kit.edu

Other Authors

Bingsheng Qin – Helmholtz Institute Ulm (HIU)
Electrochemical Energy Storage, Ulm, Germany, and
Karlsruhe Institute of Technology (KIT), Karlsruhe,
Germany

Alexander Schiele – Karlsruhe Institute of Technology
(KIT), Eggenstein-Leopoldshafen, Germany

Zenonas Jusys – Ulm University, Ulm, Germany

Alessandro Mariani – Helmholtz Institute Ulm (HIU)
Electrochemical Energy Storage, Ulm, Germany, and
Karlsruhe Institute of Technology (KIT), Karlsruhe,
Germany

Thomas Diemant – Ulm University, Ulm, Germany

Xu Liu – Helmholtz Institute Ulm (HIU) Electrochemical
Energy Storage, Ulm, Germany, and Karlsruhe Institute of
Technology (KIT), Karlsruhe, Germany; orcid.org/0000-0003-0532-316X

Torsten Brezesinski – Karlsruhe Institute of Technology
(KIT), Eggenstein-Leopoldshafen, Germany; orcid.org/0000-0002-4336-263X

R. Jürgen Behm – Helmholtz Institute Ulm (HIU)
Electrochemical Energy Storage, Ulm, Germany, and Ulm
University, Ulm, Germany; orcid.org/0000-0002-7565-0628

Complete contact information is available at:
<https://pubs.acs.org/10.1021/acsami.9b20616>

Notes

The authors declare no competing financial interest.

■ ACKNOWLEDGMENTS

B.Q. and X.L. gratefully acknowledge the financial support from the Chinese Scholarship Council and the Helmholtz Association. The work of Z.J. was supported by the German Federal Ministry of Education and Research (BMBF) in the project 03X4636C. Sincere thanks are given to Dr. Alexander Hoefling for the fruitful discussion. This work contributes to the research performed at CELEST (Center for Electrochemical Energy Storage Ulm Karlsruhe).

■ REFERENCES

- (1) Dunn, B.; Kamath, H.; Tarascon, J. M. Electrical Energy Storage for the Grid: A Battery of Choices. *Science* **2011**, *334*, 928–935.
- (2) Nayak, P. K.; Yang, L.; Brehm, W.; Adelhelm, P. From Lithium Ion to Sodium Ion Batteries: Advantages, Challenges, and Surprises. *Angew. Chem., Int. Ed.* **2018**, *57*, 102–120.
- (3) Obrovac, M. N.; Chevrier, V. L. Alloy Negative Electrodes for Li Ion Batteries. *Chem. Rev.* **2014**, *114*, 11444–11502.
- (4) Schiele, A.; Breitung, B.; Hatsukade, T.; Berkes, B. B.; Hartmann, P.; Janek, J.; Brezesinski, T. The Critical Role of Fluoroethylene Carbonate in the Gassing of Silicon Anodes for Lithium Ion Batteries. *ACS Energy Lett.* **2017**, *2*, 2228–2233.
- (5) Lao, M.; Zhang, Y.; Luo, W.; Yan, Q.; Sun, W.; Dou, S. X. Alloy Based Anode Materials toward Advanced Sodium Ion Batteries. *Adv. Mater.* **2017**, *29*, 1700622.

- (6) Sultana, I.; Rahman, M. M.; Chen, Y.; Glushenkov, A. M. Potassium Ion Battery Anode Materials Operating through the Alloying–Dealloying Reaction Mechanism. *Adv. Funct. Mater.* **2018**, *28*, 1703857.
- (7) Zhang, H.; Hasa, I.; Passerini, S. Beyond Insertion for Na Ion Batteries: Nanostructured Alloying and Conversion Anode Materials. *Adv. Energy Mater.* **2018**, *8*, 1702582.
- (8) Schiele, A.; Breitung, B.; Mazilkin, A.; Schweidler, S.; Janek, J.; Gumbel, S.; Fleischmann, S.; Burakowska Meise, E.; Sommer, H.; Brezesinski, T. Silicon Nanoparticles with a Polymer Derived Carbon Shell for Improved Lithium Ion Batteries: Investigation into Volume Expansion, Gas Evolution, and Particle Fracture. *ACS Omega* **2018**, *3*, 16706–16713.
- (9) Aurbach, D. Review of Selected Electrode–Solution Interactions Which Determine the Performance of Li and Li Ion Batteries. *J. Power Sources* **2000**, *89*, 206–218.
- (10) Li, S.; Niu, J.; Zhao, Y. C.; So, K. P.; Wang, C.; Wang, C. A.; Li, J. High Rate Aluminium Yolk shell Nanoparticle Anode for Li ion Battery with Long Cycle Life and Ultrahigh Capacity. *Nat. Commun.* **2015**, *6*, 7872.
- (11) Tie, D.; Huang, S.; Wang, J.; Ma, J.; Zhang, J.; Zhao, Y. Hybrid Energy Storage Devices: Advanced Electrode Materials and Matching Principles. *Energy Storage Mater.* **2019**, *21*, 22–40.
- (12) Zhang, B.; Rousse, G.; Foix, D.; Dugas, R.; Corte, D. A. D.; Tarascon, J. M. Microsized Sn as Advanced Anodes in Glyme Based Electrolyte for Na Ion Batteries. *Adv. Mater.* **2016**, *28*, 9824–9830.
- (13) Li, Z.; Ding, J.; Mitlin, D. Tin and Tin Compounds for Sodium Ion Battery Anodes: Phase Transformations and Performance. *Acc. Chem. Res.* **2015**, *48*, 1657–1665.
- (14) Kim, C.; Kim, I.; Kim, H.; Sadan, M. K.; Yeo, H.; Cho, G.; Ahn, J.; Ahn, J.; Ahn, H. A Self Healing Sn Anode with An Ultra Long Cycle Life for Sodium Ion Batteries. *J. Mater. Chem. A* **2018**, *6*, 22809–22818.
- (15) Wang, L.; Ni, Y.; Lei, K.; Dong, H.; Tian, S.; Li, F. 3D Porous Tin Created by Tuning the Redox Potential Acts as an Advanced Electrode for Sodium Ion Batteries. *ChemSusChem* **2018**, *11*, 3376–3381.
- (16) Wang, C.; Wang, L.; Li, F.; Cheng, F.; Chen, J. Bulk Bismuth as a High Capacity and Ultralong Cycle Life Anode for Sodium Ion Batteries by Coupling with Glyme Based Electrolytes. *Adv. Mater.* **2017**, *29*, 1702212.
- (17) Song, M.; Wang, C.; Du, D.; Li, F.; Chen, J. A High Energy Density Sodium Ion Full Battery Based on Tin Anode. *Sci. China: Chem.* **2019**, *62*, 616–621.
- (18) Wang, C.; Du, D.; Song, M.; Wang, Y.; Li, F. A High Power $\text{Na}_3\text{V}_2(\text{PO}_4)_3$ Bi Sodium Ion Full Battery in a Wide Temperature Range. *Adv. Energy Mater.* **2019**, *9*, 1900022.
- (19) Lei, K.; Wang, C.; Liu, L.; Luo, Y.; Mu, C.; Li, F.; Chen, J. A Porous Network of Bismuth Used as the Anode Material for High Energy Density Potassium Ion Batteries. *Angew. Chem., Int. Ed.* **2018**, *57*, 4687–4691.
- (20) Li, K.; Zhang, J.; Lin, D.; Wang, D. W.; Li, B.; Lv, W.; Sun, S.; He, Y. B.; Kang, F.; Yang, Q. H.; Zhou, L.; Zhang, T. Y. Evolution of the Electrochemical Interface in Sodium Ion Batteries with Ether Electrolytes. *Nat. Commun.* **2019**, *10*, 725.
- (21) Huang, J.; Guo, X.; Du, X.; Lin, X.; Huang, J. Q.; Tan, H.; Zhu, Y.; Zhang, B. Nanostructures of solid electrolyte interphases and their consequences for microsized Sn anodes in sodium ion batteries. *Energy Environ. Sci.* **2019**, *12*, 1550–1557.
- (22) Raccichini, R.; Amores, M.; Hinds, G. Critical Review of the Use of Reference Electrodes in Li Ion Batteries: A Diagnostic Perspective. *Batteries* **2019**, *5*, 12.
- (23) Liu, X.; Qin, B.; Zhang, H.; Moretti, A.; Passerini, S. Glyme Based Electrolyte for Na/Bilayered V_2O_5 Batteries. *ACS Appl. Energy Mater.* **2019**, *2*, 2786–2793.
- (24) Gantenbein, S.; Weiss, M.; Ivers Tiffée, E. Impedance Based Time Domain Modeling of Lithium Ion Batteries: Part I. *J. Power Sources* **2018**, *379*, 317–327.
- (25) Qin, B.; Diemant, T.; Zhang, H.; Hoefling, A.; Behm, R. J.; Tübke, J.; Varzi, A.; Passerini, S. Revisiting the Electrochemical Lithiation Mechanism of Aluminum and the Role of Li rich Phases (Li_{1+x}Al) on Capacity Fading. *ChemSusChem* **2019**, *12*, 2609–2619.
- (26) Qin, B.; Zhang, H.; Diemant, T.; Geiger, D.; Raccichini, R.; Behm, R. J.; Kaiser, U.; Varzi, A.; Passerini, S. Ultrafast Ionic Liquid Assisted Microwave Synthesis of SnO Microflowers and Their Superior Sodium Ion Storage Performance. *ACS Appl. Mater. Interfaces* **2017**, *9*, 26797–26804.
- (27) Qin, B.; Jeong, S.; Zhang, H.; Ulissi, U.; Vieira Carvalho, D.; Varzi, A.; Passerini, S. Enabling Reversible (De)Lithiation of Aluminum by using Bis(fluorosulfonyl)imide Based Electrolytes. *ChemSusChem* **2018**, *12*, 208–212.
- (28) Eshetu, G. G.; Diemant, T.; Grugeon, S.; Behm, R. J.; Laruelle, S.; Armand, M.; Passerini, S. In Depth Interfacial Chemistry and Reactivity Focused Investigation of Lithium Imide and Lithium Imidazole Based Electrolytes. *ACS Appl. Mater. Interfaces* **2016**, *8*, 16087–16100.
- (29) Xu, G.; Wang, X.; Li, J.; Shangguan, X.; Huang, S.; Lu, D.; Chen, B.; Ma, J.; Dong, S.; Zhou, X.; Kong, Q.; Cui, G. Tracing the Impact of Hybrid Functional Additives on a High Voltage (5 V class) $\text{SiO}_x\text{C}/\text{LiNi}_{0.5}\text{Mn}_{1.5}\text{O}_4$ Li Ion Battery System. *Chem. Mater.* **2018**, *30*, 8291–8302.
- (30) Jozwiuk, A.; Berkes, B. B.; Weiß, T.; Sommer, H.; Janek, J.; Brezesinski, T. The critical role of lithium nitrate in the gas evolution of lithium sulfur batteries. *Energy Environ. Sci.* **2016**, *9*, 2603–2608.
- (31) Jusys, Z.; Binder, M.; Schnaidt, J.; Behm, R. J. A Novel DEMS Approach for Studying Gas Evolution at Battery Type Electrode/Electrolyte Interfaces: High voltage $\text{LiNi}_{0.5}\text{Mn}_{1.5}\text{O}_4$ Cathode in Ethylene and Dimethyl Carbonate Electrolytes. *Electrochim. Acta* **2019**, *314*, 188–201.
- (32) Westman, K.; Dugas, R.; Jankowski, P.; Wiczorek, W.; Gachot, G.; Morcrette, M.; Irisarri, E.; Ponrouch, A.; Palacin, M. R.; Tarascon, J. M.; Johansson, P. Diglyme Based Electrolytes for Sodium Ion Batteries. *ACS Appl. Energy Mater.* **2018**, *1*, 2671–2680.
- (33) Bridel, J. S.; Grugeon, S.; Laruelle, S.; Hassoun, J.; Reale, P.; Scrosati, B.; Tarascon, J. M. Decomposition of Ethylene Carbonate on Electrodeposited Metal Thin Film Anode. *J. Power Sources* **2010**, *195*, 2036–2043.
- (34) Tavassol, H.; Buthker, J. W.; Ferguson, G. A.; Curtiss, L. A.; Gewirth, A. A. Solvent Oligomerization during SEI Formation on Model Systems for Li Ion Battery Anodes. *J. Electrochem. Soc.* **2012**, *159*, A730–A738.
- (35) Shkrob, I. A.; Marin, T. W.; Zhu, Y.; Abraham, D. P. Why Bis(fluorosulfonyl)imide Is a “Magic Anion” for Electrochemistry. *J. Phys. Chem. C* **2014**, *118*, 19661–19671.
- (36) Piper, D. M.; Evans, T.; Leung, K.; Watkins, T.; Olson, J.; Kim, S. C.; Han, S. S.; Bhat, V.; Oh, K. H.; Buttry, D. A.; Lee, S. H. Stable Silicon Ionic Liquid Interface for Next Generation Lithium Ion Batteries. *Nat. Commun.* **2015**, *6*, 6230.
- (37) Markevich, E.; Salitra, G.; Aurbach, D. Fluoroethylene Carbonate as an Important Component for the Formation of an Effective Solid Electrolyte Interphase on Anodes and Cathodes for Advanced Li Ion Batteries. *ACS Energy Lett.* **2017**, *2*, 1337–1345.
- (38) Soto, F. A.; Yan, P.; Engelhard, M. H.; Marzouk, A.; Wang, C.; Xu, G.; Chen, Z.; Amine, K.; Liu, J.; Sprenkle, V. L.; El Mellouhi, F.; Balbuena, P. B.; Li, X. Tuning the Solid Electrolyte Interphase for Selective Li and Na Ion Storage in Hard Carbon. *Adv. Mater.* **2017**, *29*, 1606860.
- (39) Yang, Z.; Gewirth, A. A.; Trahey, L. Investigation of Fluoroethylene Carbonate Effects on Tin based Lithium Ion Battery Electrodes. *ACS Appl. Mater. Interfaces* **2015**, *7*, 6557–6566.
- (40) Schiele, A.; Hatsukade, T.; Berkes, B. B.; Hartmann, P.; Brezesinski, T.; Janek, J. High Throughput in Situ Pressure Analysis of Lithium Ion Batteries. *Anal. Chem.* **2017**, *89*, 8122–8128.
- (41) Berkes, B. B.; Jozwiuk, A.; Sommer, H.; Brezesinski, T.; Janek, J. Simultaneous Acquisition of Differential Electrochemical Mass Spectrometry and Infrared Spectroscopy Data for in situ Characterization of Gas Evolution Reactions in Lithium Ion Batteries. *Electrochem. Commun.* **2015**, *60*, 64–69.
- (42) Berkes, B. B.; Jozwiuk, A.; Vračar, M.; Sommer, H.; Brezesinski, T.; Janek, J. Online Continuous Flow Differential Electrochemical Mass

Spectrometry with a Realistic Battery Setup for High Precision, Long Term Cycling Tests. *Anal. Chem.* **2015**, *87*, 5878–5883.